Acta Materialia 187 (2020) 112–121

Contents lists available at ScienceDirect

Acta Materialia

journal homepage: www.elsevier.com/locate/actamat

Full length article

Facile healing of cracks in organic–inorganic halide perovskite thin films

Srinivas K. Yadavalli[a], Zhenghong Dai[a], Hua Zhou[b], Yuanyuan Zhou[a], Nitin P. Padture[a,*]

[a] School of Engineering, Brown University, Providence, RI 02912, USA
[b] Advanced Photon Source, Argonne National Laboratory, Lemont, IL 60439, USA

ARTICLE INFO

Article History:
Received 10 September 2019
Revised 27 November 2019
Accepted 19 January 2020
Available online 24 January 2020

Keywords:
Halide perovskite
Thin film
Crack healing
X-ray diffraction
Scanning electron microscopy

ABSTRACT

Organic–inorganic halide perovskite (OIHP) thin films at the heart of the burgeoning thin-film perovskite solar cells (PSCs) technology possess poor mechanical properties, which is likely to limit the long-term reliability of PSCs as they are poised for commercialization. In an effort to address this issue, here we demonstrate that through-thickness cracks induced by bending-tension in thin films of the two prototypical OIHPs, methylammonium lead triiodide ($MAPbI_3$) and formamidinium lead triiodide ($FAPbI_3$), can be healed easily. This is through the application of either a moderate compressive stress (bending-compression) at room temperature or a simple heat-treatment at modest temperatures. The crack-healing process is found to be time-dependent, which indicates that facile mass-transport in OIHPs plays a key role in this phenomenon. An explanation for this phenomenon is provided, one based on the fundamentals of brittle fracture. This discovery has broad implications for the prevention and/or restoration of the overall performance, environmental stability, and mechanical reliability of PSCs, and other devices.

1. Introduction

Organic–inorganic halide perovskites (OIHPs), at the heart of the burgeoning thin-film thin-film perovskite solar cells (PSCs) technology, are a fascinating family of true hybrid materials with unprecedented optoelectronic and defect-tolerance properties [1–5]. As such, there is widespread interest in PSCs where the record efficiency has now topped 25% [6], rivaling silicon photovoltaics (PVs). Another important feature of OIHP thin films driving the interest in PSCs, and for other potential applications of OIHPs [7], including light-emitting diodes [8], lasers [9], and detectors [10–12], is that they can be deposited using low-cost solution-based methods [13]. This is due to their low formation energies [14,15], but this also makes OIHPs unstable [16,17]. Thus, much of research in the PSCs field has expanded to improving not only performance [2,4,5] and scalability [18], but also stability [16,17], where significant progress has been made. However, PSCs will also need to be mechanically reliable if they are to operate efficiently for decades, but there is paucity of research in this area [16,19–22]. This is particularly important in the case of PSCs because OIHPs, owing to their low formation energies, are also inherently compliant (low Young's modulus, E), soft (low hardness, H), and brittle (low fracture toughness, K_{IC}) [19,21–24]. For example, $MAPbI_3$ has E~17.8 GPa, H~0.58 GPa, and K_{IC}~0.22 MPa $m^{0.5}$ [21]. By comparison, silicon, the workhorse material used in myriad devices including PVs, has E~170 GPa, H~10 GPa, and K_{IC}~0.7 MPa $m^{0.5}$ [25]. However, the critical strain energy release rate, $G_C = K_{IC}^2/E$, also referred to as toughness or cohesion energy, is similar for the two materials: $MAPbI_3$ G_C~2.7 J m^{-2} and silicon G_C~2.9 J m^{-2}. The sources of mechanical stresses that drive fracture in OIHP thin films within the multilayer PSCs include: (i) internal residual stresses due the coefficient of thermal expansion (CTE) mismatch with the substrate and other layers; (ii) thermo-mechanical stresses due to in-service thermal excursions; and (iii) externally applied stresses, *e.g.* bending, stretching, twisting of flexible devices.

It is noteworthy that, historically, most commercial devices, including PVs, have gone through a familiar research/development sequence – increasing performance, upscaling, improving stability, and enhancing reliability – before making it to the marketplace successfully. In this context, PSCs are likely to be no exception. Thus, to address some of the issues related to enhancing reliability, here we report the first demonstration of facile healing of through-thickness cracks in thin films of two prototypical OIHPs, methylammonium lead triiodide ($CH_3NH_3PbI_3$ or $MAPbI_3$) and formamidinium lead triiodide (α-$HC(NH_2)_2PbI_3$ or α-$FAPbI_3$), that can be deleterious to their properties. This is through the application of either a moderate compressive stress at room temperature or a simple heat-treatment at moderate temperatures. Thus, while OIHP thin films crack readily because of their brittleness, they can also be healed readily – a discovery that has broad implications for the prevention and/or restoration of the overall performance, environmental stability, and mechanical reliability of PSCs, and other devices, as they are poised for commercialization.

* Corresponding author.
E-mail address: nitin_padture@brown.edu (N.P. Padture).

https://doi.org/10.1016/j.actamat.2020.01.040
1359-6454/

2. Experimental procedure

2.1. Thin film synthesis

$MAPbI_3$ thin films (~400 nm thickness) were synthesized using the solvent-engineering method [26]. Briefly, the $MAPbI_3$ precursor solution was prepared by dissolving MAI (Greatcell, Australia) and PbI_2 (Alfa Aesar, USA) in stoichiometric (1:1) ratio in dimethyl formamide (DMF; Sigma Aldrich, USA) to obtain a 40 wt% solution. Polyethylene terephthalate (PET) substrates (15 × 15 mm^2, ~178 μm thickness) coated with indium-doped tin oxide (ITO; ~100 nm thickness) transparent-conducting oxide (TCO) obtained commercially (Sigma Aldrich, USA) were first cleaned. The precursor solution was spin-coated onto the substrates at 4000 rpm for 20 s, during which 250 μL of antisolvent chlorobenzene (Sigma Aldrich, USA) was dripped quickly at the end of 6^{th} second at the center of the film. The resulting films were heat-treated using a hotplate at 115 °C for 10 min, to result in fully-crystallized standard $MAPbI_3$ thin films used in this study. In order to study the effect of the ITO coating on the PET substrate, some $MAPbI_3$ thin films were deposited on bare PET substrates without the ITO coating using the same procedure.

α-$FAPbI_3$ OIHP thin films (~500 nm thickness) were synthesized using a method reported elsewhere [27]. Briefly, the $FAPbI_3$ precursor solution was prepared by dissolving 0.086 g FAI (Greatcell, Australia) and 0.23 gm PbI_2 (Alfa Aesar, USA) in a mixture of 0.29 g DMF (Acros Organics, USA) and 47 μL of n-methyl-2 pyrrolidinone (NMP; Acros Organics, USA). The precursor solution was spin-coated on pre-cleaned ITO/PET substrates at 4000 rpm for 30 s, during which 130 μL of antisolvent diethyl ether (DEE; Sigma Aldrich, USA) was dripped quickly at the end of 8^{th} second at the center of the film. The resulting films were heat-treated using a hotplate at 80 °C for 1 min, followed by 160 °C for 10 min, to result in the standard α-$FAPbI_3$ thin films used in this study.

All thin-film synthesis was performed in a N_2-filled glovebox.

2.2. Scanning electron microscopy (SEM)

Fig. 1 shows the overall scheme for the cracking and healing experiments. The as-synthesized, cracked, mechanically-healed, and thermally-healed OIHP thin films, corresponding to states I, II, III, and IV in Fig. 1, respectively, were observed in a SEM (LEO, Zeiss, Germany) operated at 5KV accelerating voltage. SEM imaging was performed using a prolonged *e*-beam exposure of ~3 min, as explained later in Section 3.1. Some rapid SEM observations were also performed by limiting the *e*-beam exposure to few seconds. In some cases, ITO/PET substrates by themselves, and ones with $MAPbI_3$ thin films, were also observed in the SEM *in situ* while under the bending-tension (see Fig. S1 in Supporting Materials (SM)).

2.3. Mechanical testing

The OIHP thin films on ITO/PET substrates were subjected to a uniform stress by wrapping them around a glass mandrel of known radii (R), as shown in Fig. S1 in SM. This procedure, rather than bending the substrate without the mandrel, ensures constant bending radius over the entire specimen and, thus, a uniform applied uniaxial stress. This applied stress is either tensile (σ_T) or compressive (σ_C) when the curvature is positive (OIHP film facing the outside) or negative (OIHP film facing inside, in contact with the mandrel), respectively. Fig. 2(A) shows SEM images of $MAPbI_3$ thin film while under bending (R = 7.4 mm) with 'channeling' cracks. Under the same conditions, the bare ITO of the ITO/PET substrate, without the $MAPbI_3$ thin film,

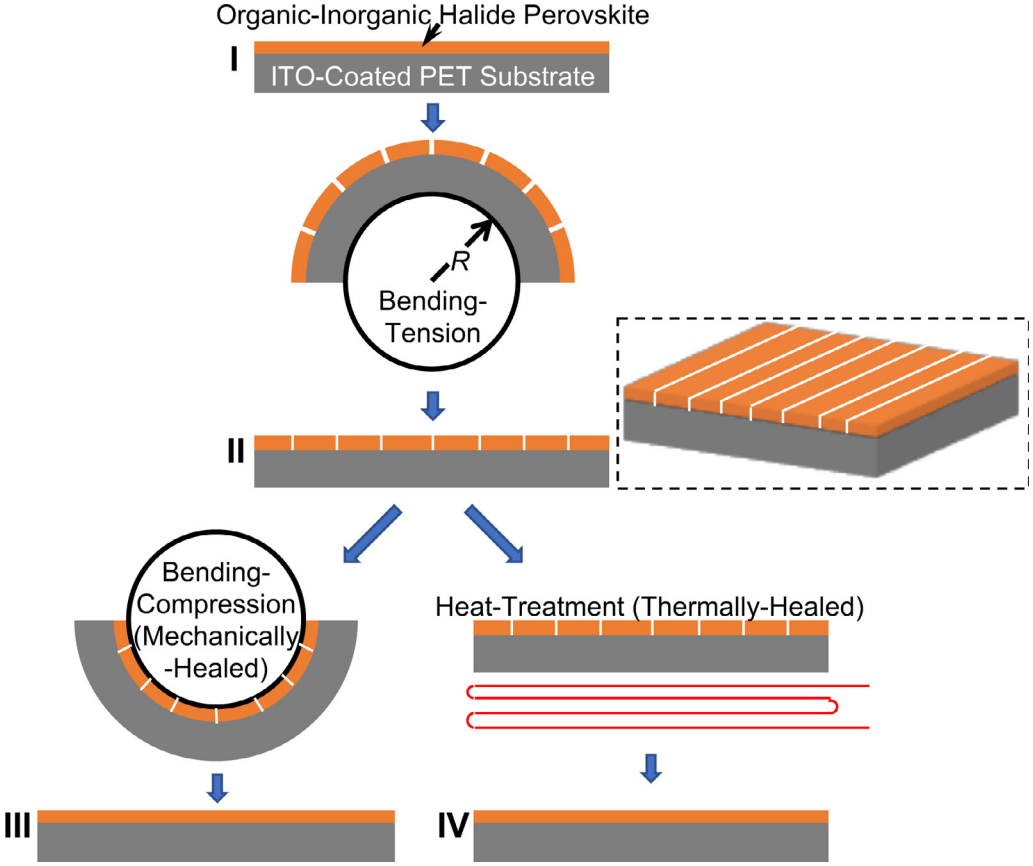

Fig. 1. Schematic illustration (cross-sectional) of the procedures used for the cracking and crack-healing in OIHP thin films (400–500 nm thickness) on flexible ITO/PET substrates (~180 μm thickness): (I) as-synthesized, (II) cracked, (III) mechanically-healed, and (IV) thermally-healed. 3D schematic illustration of II included (right). Not to scale.

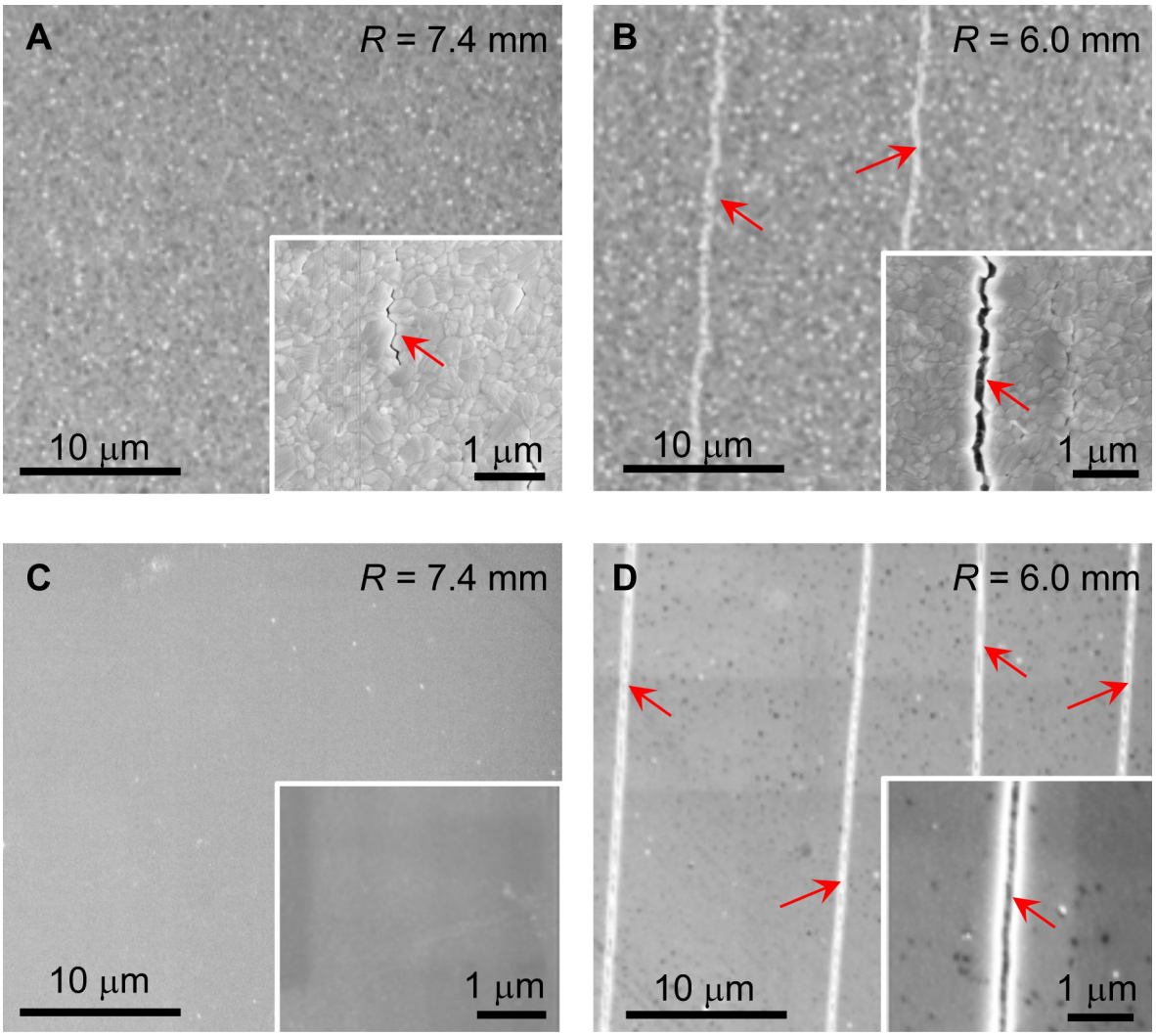

Fig. 2. Top-surface SEM images of $MAPbI_3$ thin film while under tension-bending (see Fig. S1 in SM) at: (A) R = 7.4 mm and (B) R = 6.0 mm. Top-surface SEM images of bare ITO/PET substrates while under bending-tension at: (C) R = 7.4 mm and (D) R = 6.0 mm. Insets: higher magnification images. 'Channeling' cracks marked by arrows.

does not show cracking (Fig. 2(C)). This implies that the 'channeling' cracks are confined to the $MAPbI_3$ thin film. At sharper bending radius (R = 6.0 mm) both the $MAPbI_3$ thin film (Fig. 2(B)) and the bare ITO of the ITO/PET substrate (Fig. 2(D)) show extensive channeling-cracking. Thus, in Fig. 2(B) and (D) it appears that the cracking of the ITO in the ITO/PET substrate governs the cracking of the $MAPbI_3$ thin film above. Therefore, the bending radius was limited to R = 7.4 mm in this study, where this applied bending-tension (for 0.5 min) corresponds to a uniaxial tensile stress of σ_T = 214 MPa in the OIHP thin film, calculated using:

$$\sigma_T = \frac{Eh}{2R}, \tag{1}$$

where E = 17.8 for $MAPbI_3$ [21] and h = 178 μm (neglecting the extremely thin ITO and OIHP films). In the case of α-$FAPbI_3$, reliable mechanical properties data are scarce, but they are not expected to be substantially different from that of $MAPbI_3$ as the mechanical behavior of OIHPs is governed primarily by the 3D framework inorganic of the (PbI_6^{4-}) octahedra, where the Pb-I bond distance in both OIHPs is almost the same [24]. Therefore, the same E = 17.8 GPa is assumed for α-$FAPbI_3$ thin film for calculating σ_T and σ_C.

For mechanical-healing, the mandrel radius was R = 7.4 mm (σ_C = −214 MPa), and the duration was 0.5 min. In order to expand the mechanical-healing timescale for studying possible time-dependent effects, a shallower R = 13.5 mm was used for bending-compression (σ_C = −117 MPa) for 0.5 min and 1 min, while the same R = 7.4 mm for bending-tension (σ_T = 214 MPa, 0.5 min) was used to induce cracking beforehand.

For thermal-healing, the heat-treatment conditions for $MAPbI_3$ and α-$FAPbI_3$ thin films were 100 °C for 5 min and 140 °C for 10 min, respectively. To study the time dependence of thermal healing effect in $MAPbI_3$ thin films, a lower annealing temperature (80 °C) was used, and the residual stress was measured as a function of time.

2.4. X-ray diffraction

The as-synthesized $MAPbI_3$ and α-$FAPbI_3$ thin films were characterized using a laboratory diffractometer (Cu K_α radiation; D8 Discover, Bruker, Germany) in ambient atmosphere to confirm their phase purity. The equi-biaxial residual tensile stresses (σ_R) in the $MAPbI_3$ thin films in the various states (I, II, III, and IV) were measured at room temperature using the well-established and internally-consistent $\sin^2\psi$ method. Here XRD patterns were collected using the same diffractometer as a function angle ψ, which is perpendicular to the axes normal to the scattering and the specimen planes. The d-spacings for the well-defined (224) Bragg peak at the 2θ–40.6° were used to generate the d-spacing *vs.* $\sin^2\psi$ plots. The residual

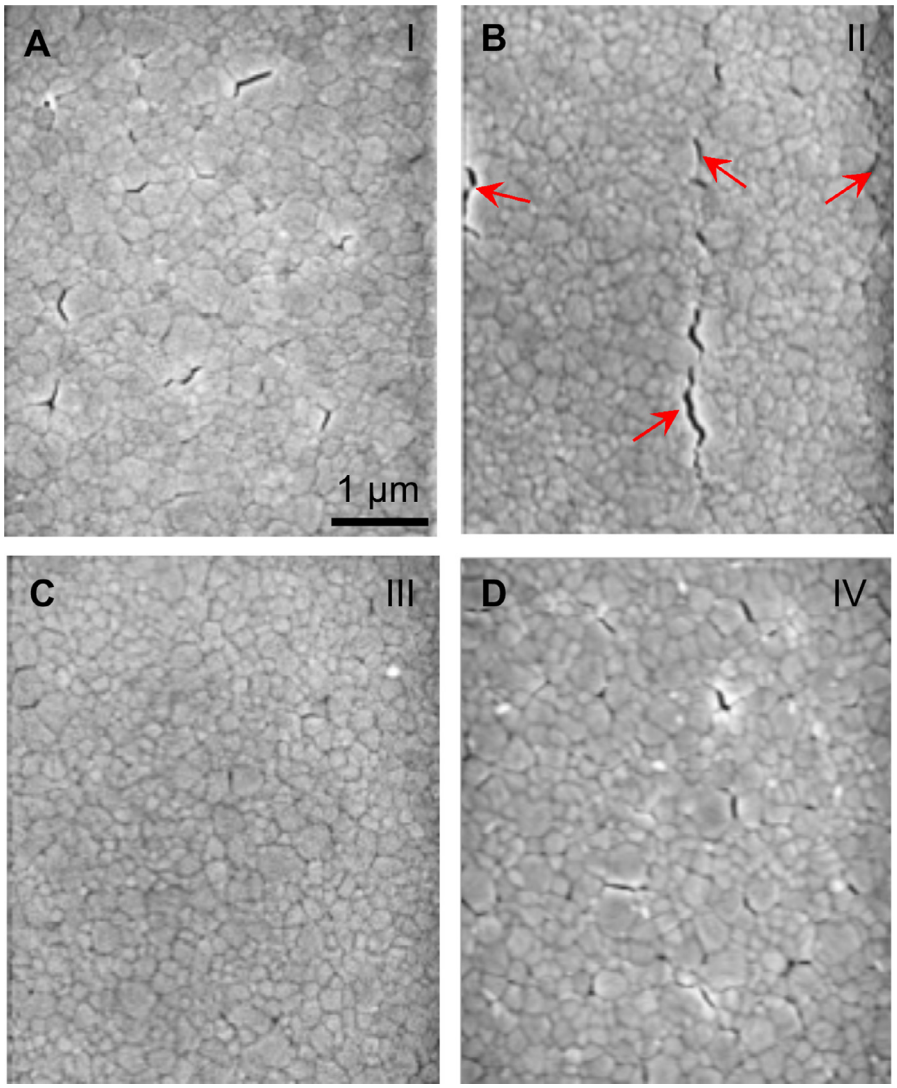

Fig. 3. Top-surface SEM images of $MAPbI_3$ thin films corresponding to the various states: (A) as-synthesized (I), (B) cracked (II), (C) mechanically-healed (III), and (D) thermally-healed (IV). Arrows in (B) mark 'channeling' cracks. SEM *e*-beam exposure is ~3 min, and the accelerating voltage is 5 kV. See Figs. S4A-S4C in SM for corresponding SEM images (same regions) for few seconds SEM *e*-beam exposure.

stress is calculated using the following relation [28,29]:

$$\sigma_R = \left(\frac{E}{1+\nu}\right)_{\langle 224\rangle}\left(\frac{m}{d_n}\right), \quad (2)$$

where m is the slope of the linear fit to the data in Fig. S2(A)–S2(D) in SM, d_n is the d_{224} spacing at $\psi = 0$ (y-intercept), E is the Young's modulus, and ν is the Poisson's ratio. Since the elastic constants of $MAPbI_3$ in the $\langle 224\rangle$ directions are not known, the average values for E (=17.8 GPa) [21] and ν (=0.33) [23] are used, which is a good approximation considering that {224} are high-index planes. In the case of α-$FAPbI_3$ thin films, since m~0 in Fig. S3 in SM ((003) Bragg peak at 2θ~40.3°), σ_R is assumed to be negligible.

As-synthesized (state I), cracked (state II), and mechanically-healed (state III) α-$FAPbI_3$ thin films were exposed to 80% relative humidity (RH) at 23 °C for 12 and 18 h. XRD patterns of these thin films were obtained using the laboratory diffractometer to study their degradation.

In order to confirm the mechanical-healing effect in a $MAPbI_3$ thin film, synchrotron grazing-incidence wide-angle X-ray scattering (GIWAXS) measurements were carried out at the undulator beamline sector 12-ID-D of the Advanced Photon Source at Argonne National Laboratory. The sample was mounted on a Huber six-circle

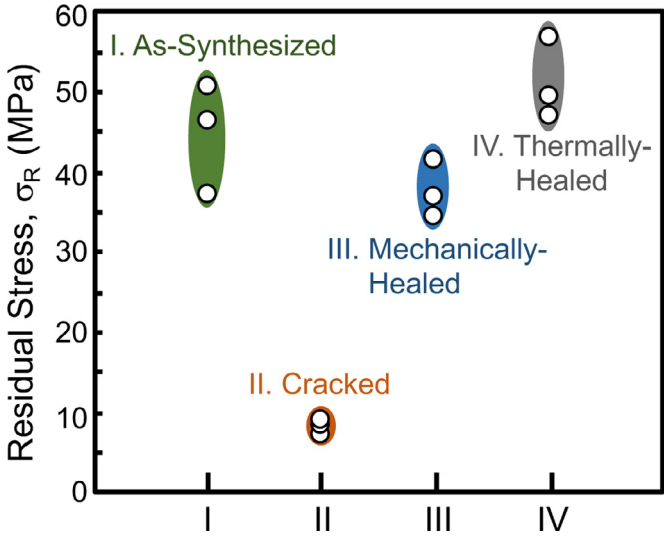

Fig. 4. Measured σ_R in $MAPbI_3$ thin films corresponding to states I, II, III, and IV. Each circle is an individual measurement.

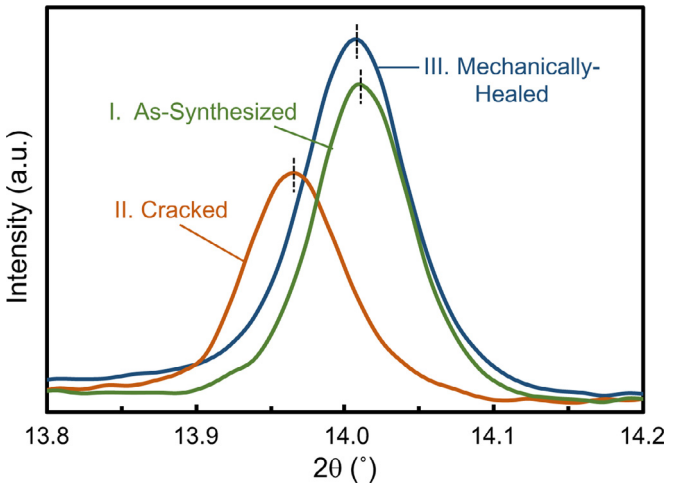

Fig. 5. Synchrotron XRD patterns (same Intensity scale) from a $MAPbI_3$ thin film ((110) Bragg peak) corresponding to the various states: (I) as-synthesized, (II) cracked, and (III) mechanically-healed.

diffractometer that can precisely control the X-ray angle of incidence to achieve the grazing incidence condition for GIWAXS. The thin-film Bragg peak intensity was used to align the optimal angle of incidence. All GIWAXS measurements were conducted at room temperature at X-ray energy of 20 keV, with the beam profile of 500 μm (horizontal) × 70 μm (vertical). An optical laser alignment was utilized to locate the same X-ray spot and footprint between different states (I, II, and III) on the same $MAPbI_3$ thin film.

3. Results

3.1. $MAPbI_3$ thin films

Fig. 3(A) is a top-surface SEM image of the as-synthesized $MAPbI_3$ thin film (state I) after prolonged *e*-beam exposure. A few grain-boundary micro-cracks of random orientation are observed. Fig. 3(B) is a SEM image of the $MAPbI_3$ thin film top-surface after applying bending-tension (σ_T = 214 MPa, 0.5 min) and flattening the sample (state II), where oriented large 'channeling' cracks are seen upon prolonged *e*-beam exposure. After bending-compression (mechanical-healing) the same $MAPbI_3$ thin film (σ_C = −214 MPa, 0.5 min), and then flattening the sample (state III), the cracks appear to have been healed (Fig. 3(C)). These same experiments were repeated at several arbitrary locations within a region (~0.1 × 0.12 mm^2) before and after healing the cracked $MAPbI_3$ thin film specimen, and also repeated in several different specimens, where similar SEM results were obtained in all the cases.

It should be pointed out that during the SEM observation of OIHP thin films, micro-cracking is often seen to occur, even at the low accelerating voltage of 5 KV. Typically, the micro-cracking is limited to opening up random grain boundaries in the as-synthesized thin films. In Fig. S4(A) in SM the top and bottom images show the same area of an as-synthesized $MAPbI_3$ thin film (state I) after 0 min and 3 min exposure to the SEM *e*-beam, respectively. While no grain-boundary micro-cracks are observed in the top image, they open up in random orientations, and are marked in the bottom image. In the case of cracked $MAPbI_3$ thin film (state II) in Fig. S4B in SM, after 3 min SEM *e*-beam exposure (bottom), oriented cracks ('channeling' cracks) appear, although they are not visible in the top image (few-seconds SEM *e*-beam exposure). In the case of the mechanically-healed film (state III), no 'channeling' cracks are visible, only random grain-boundary micro-cracks are observed in Fig. S4(C) (bottom) in SM, similar to the as-synthesized thin film (Fig. S4(A) (bottom) in SM). Thus, the SEM *e*-beam exposure leads to grain-boundary micro-cracks in the as-synthesized and the healed $MAPbI_3$ thin films, and opens up preexisting 'channeling' cracks in the cracked $MAPbI_3$ thin film. The SEM *e*-beam-induced delineation of preexisting cracks is also observed in α-$FAPbI_3$, but it is typically not observed in all-inorganic halide perovskites, such as $CsPbI_3$. The origin of this interesting and useful phenomenon is related to the partial volatilization of the organic molecules (MAI or FAI) under the SEM *e*-beam due to knock-on damage [30]. This results in volume shrinkage of the grains that pull away, generating local tensile stresses that help generate micro-cracks or open up the preexisting 'channeling' cracks. Unfortunately, this approach is 'destructive,' making it impossible to image the same area through the cracking and crack-healing cycle *in situ* or *ex situ*.

While SEM observations are useful, they are qualitative, highly localized, and limited to the surface, which limits the ability to delineate cracking and healing clearly. Note that, electrical-conductivity measurement is also unable to differentiate between cracks that are closed (crack walls in physical contact) and cracks that are truly healed (chemical bonding of crack walls). In this context, the manifestation of true crack-healing is the ability of the healed material to sustain large-scale tensile stresses. Here, we make use of the fact that most $MAPbI_3$ thin films are under moderate equi-biaxial in-plane tensile residual stress (σ_R) as a result of the large CTE mismatch with the substrate and cooling from the processing temperature [21]. The average linear CTEs of $MAPbI_3$ and the ITO/PET substrate are α_{OIHP}~50 × $10^{-6}°C^{-1}$ [31] and $\alpha_{ITO/PET}$~12 × 10^{-6} $°C^{-1}$ [32], respectively. Thus, a tensile σ_R~93 MPa is calculated using:

$$\sigma_R = \frac{E\Delta\alpha\Delta T}{1-\nu}, \tag{3}$$

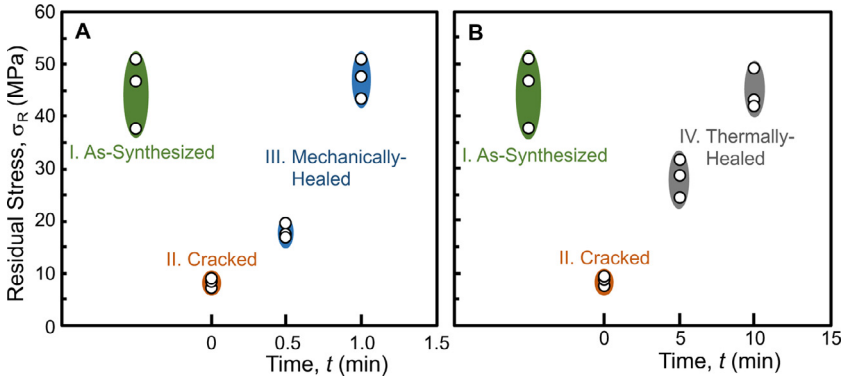

Fig. 6. Measured tensile residual stress in $MAPbI_3$ thin films as a function of healing duration: (A) mechanically-healed (III) at a lower σ_C = −117 MPa and (B) thermally-healed (IV) at a lower temperature T = 80 °C. Note the time-dependence of the crack-healing process in both cases. The as-synthesized (I) and cracked (II) data are from Fig. 4. Each circle is an individual measurement.

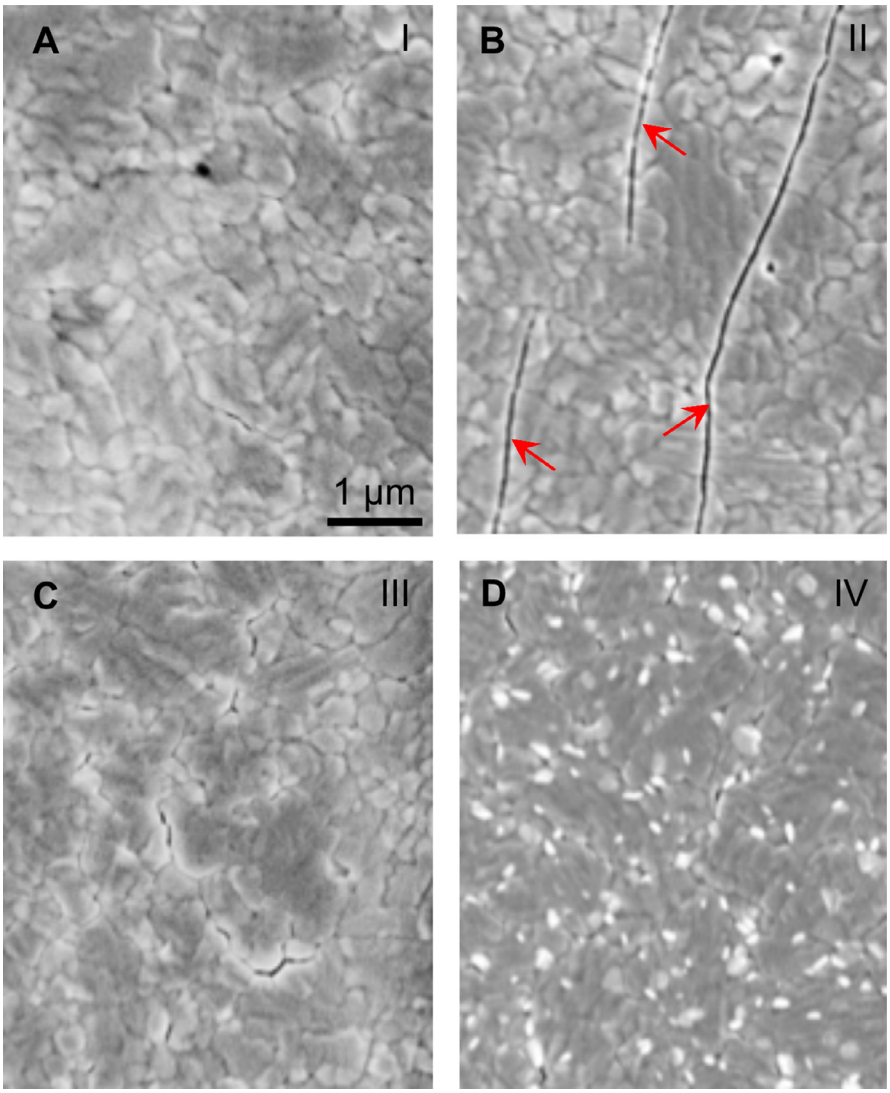

Fig. 7. Top-surface SEM images of α-$FAPbI_3$ thin films corresponding to the various states: (A) as-synthesized (I), (B) cracked (II), (C) mechanically-healed (II), and d) thermally-healed (IV). Arrows in (B) mark 'channeling' cracks. SEM *e*-beam exposure is ~3 min, and the accelerating voltage is 5 kV.

where $\Delta\alpha = \alpha_{OIHP}$-$\alpha_{ITO/PET} = 38 \times 10^{-6}$ °C^{-1}, $\Delta T = 92$ °C (115–23 °C), and ν=0.33 [21–23]. This is assuming that the crystallization of the film from the solution and its chemically-bonding to the substrate occur at the heat-treatment temperature, and that there is no stress-relaxation during cooling.

The residual stresses in the $MAPbI_3$ thin films in states I, II, III, and IV measured over a large area using the XRD $\sin^2\psi$ method are plotted in Fig. 4. An σ_R~45 MPa is found in the as-synthesized $MAPbI_3$ thin films (state I), which is lower than the calculated value of ~93 MPa. This is most likely due to the partial crystallization/attachment of the film before reaching the heat-treatment temperature. Note that a σ_R~50 MPa is measured for $MAPbI_3$ deposited on bare PET substrate without the ITO (see Fig. S5 in SM), confirming that the ITO does not play a role in determining the residual stress. The relaxation of average σ_R to ~8 MPa (average) in the cracked film (state II) is confirmed in Fig. 4. After bending-compression and flattening of the film (state III), the residual stress is mostly restored (average σ_R~38 MPa). These results confirm that the cracks have been healed, and that the film is once again able to sustain the tensile residual stresses. Fig. 5 presents the results from synchrotron XRD, where the shift of the $MAPbI_3$ Bragg peak (110) from higher 2θ~14.02° for as-synthesized film (state I) to lower 2θ~13.97° for cracked film (state II), and then back to 2θ~14.01° for mechanically-healed film (state III) further confirms the crack-healing effect in $MAPbI_3$.

Fig. 6(A) plots the measured σ_R in $MAPbI_3$ thin films (state II) as a function of bending-compression healing duration ($\sigma_C = -117$ MPa) where only partial recovery of σ_R (~18 MPa average) is observed at 0.5 min, and full recovery of σ_R (~47 MPa average) at 1 min. These results confirm the time-dependence of the mechanical-healing effect at room temperature, and suggest that stress-induced mass-transport (*e.g.* ionic diffusion) processes are at play during crack-healing. In this context, ionic diffusion is known to be facile in $MAPbI_3$ [33,34], with the following estimated ionic diffusivities: D_I~2.4×10^{-8} cm^2 s^{-1} (at 298 K) [35] and $D_{MA,Pb}$~4×10^{-15} cm^2 s^{-1} (at 343 K) [36]. Since diffusion is a thermally-activated process, crack-healing should be possible using heat-treatment alone. Also, upon heating, the higher CTE of the $MAPbI_3$ relative to the ITO/PET substrate will lead to net expansion of the thin film, inducing compression on the open cracks in the cracked films. Thus, the cracked $MAPbI_3$ films (state II) were subjected to a simple heat-treatment of 100 °C for 5 min (state IV). The SEM image in Fig. 3(D) shows healed cracks after heat-treatment. Full restoration of the residual stress (average σ_R~51 MPa) in Fig. 4 confirms thermal-healing of cracks. Lower temperature (80 °C) heat-treatment for 5 min results in only

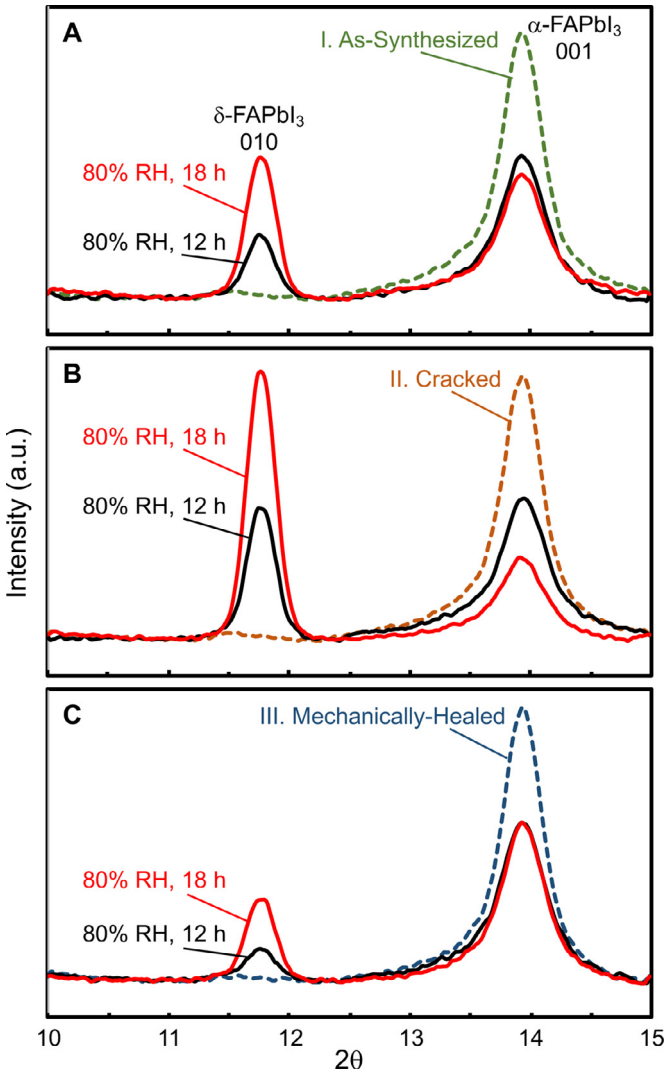

Fig. 8. XRD patterns (same Intensity scale) of α-$FAPbI_3$ thin films corresponding to the various states: (A) as-synthesized (I), (B) cracked (II), and (C) mechanically-healed (III), subjected to environmental exposure (80% RH, 23 °C) for 0 h (dashed), 12 (solid black), and 18 h (solid red). Bragg peaks for α-$FAPbI_3$ (001) and δ-$FAPbI_3$ (010) are marked.

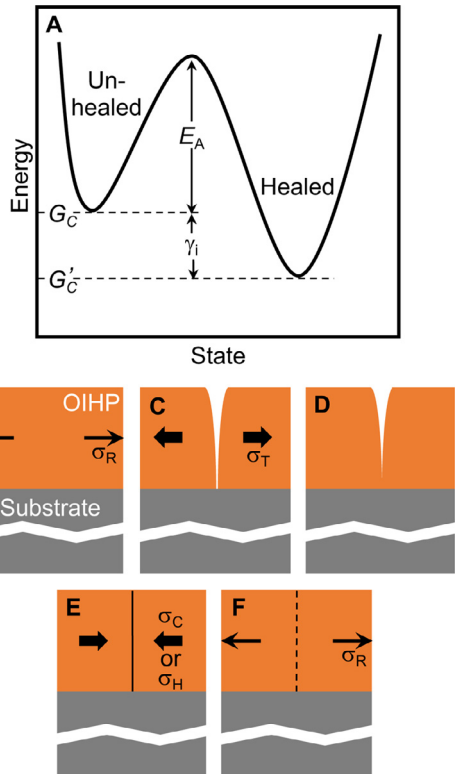

Fig. 9. (A) Schematic illustration of the energy landscape of crack-healing in brittle materials, where γ_i is the driving force for healing and E_A is the activation energy. (B)–(F) Cross-sectional schematic depiction (not to scale) of the steps in the cracking and healing (mechanical and thermal) processes, where σ_R is the tensile residual stress (in $MAPbI_3$, but not in α-$FAPbI_3$), σ_T is the applied tension (tension-bending), σ_C is the applied compression (bending-compression; mechanical-healing), and σ_H is the compression induced due to the heat-treatment (thermal-healing).

partial restoration of the residual stress (σ_R~30 MPa average), and a prolonged treatment for 10 min (80 °C) fully restores the residual stress (σ_R~44 MPa average), as seen in Fig. 6(B). This further confirms the time-dependent nature of the crack-healing process.

3.2. α-$FAPbI_3$ thin films

To investigate the generality of this phenomenon in OIHPs, the same experiments were repeated on thin films of α-$FAPbI_3$, an important OIHP material that is also being researched heavily for PSCs and other optoelectronic devices, as it has more desirable thermal stability and optical properties relative to $MAPbI_3$ [5,37]. Fig. 7 (A) is a top-view SEM image of the as-deposited α-$FAPbI_3$ thin film (state I) showing no oriented 'channeling' cracks upon prolonged *e*-beam exposure. Upon applying bending-tension (σ_T = 214 MPa, 0.5 min) and flattening the sample (state II) oriented large 'channeling' cracks are seen in Fig. 7(B) upon prolonged *e*-beam exposure. 'Channeling' Cracks in α-$FAPbI_3$ thin films propagate primarily through the grains (transgranular), whereas those in $MAPbI_3$ are mostly confined to grain boundaries (intergranular). This could be due to the CTE-anisotropy induced micro-stresses present in grain boundaries in the tetragonal $MAPbI_3$ [21], but are absent in the cubic α-$FAPbI_3$. After bending-compression (mechanical-healing) the same α-$FAPbI_3$ thin film (σ_C = −214 MPa, 0.5 min), and then flattening the sample (state III), the cracks appear to have been healed (Fig. 7(C)). In the case of thermal-healing (140 °C, 10 min), the cracks also appear to have been healed in Fig. 7(D) (state IV).

Unlike $MAPbI_3$, $FAPbI_3$ is known to exist as two polymorphs, the OIHP α-$FAPbI_3$ 'black' phase and the non-perovskite δ-$FAPbI_3$ 'yellow' phase [1]. During the processing of these thin films, the initial δ-$FAPbI_3$ attached to the substrate converts to α-$FAPbI_3$ at the heat-treatment temperature (160 °C). Associated with that δ-to-α transformation is volume expansion, where the molar volumes of the δ-$FAPbI_3$ and the α-$FAPbI_3$ phases are 255.8 $Å^3$ and 257.5 $Å^3$, respectively [38]. This translates into a linear tensile strain (ε) of ~0.0022, and due to the constraint of the substrate, results in a bi-axial residual compressive stress (σ) in the thin film of about −59 MPa (σ=$-E\varepsilon/(1-\nu)$) at the heat-treatment temperature. This negates the CTE-mismatch strain that accumulates during the cooling of the thin film to room temperature, where the α-$FAPbI_3$ is retained as a metastable phase. This is the reason for the absence of σ_R in as-deposited α-$FAPbI_3$ thin films (see Fig. S3 in SM), and hence the XRD-based σ_R measurement approach used in the case of $MAPbI_3$ thin films cannot be applied to α-$FAPbI_3$ thin films. However, the α-$FAPbI_3$ phase is known to degrade to the undesirable δ-$FAPbI_3$ 'yellow' phase upon exposure to ambient atmosphere [16,37], which is expected to be accelerated with the presence of cracks which allow facile moisture ingression. Thus, to assess the relative stabilities of as-synthesized (state I), cracked (state II), and mechanically-healed (state III) α-$FAPbI_3$ thin films, they were exposed to 80% relative humidity (RH) at 23 °C for 12 and 18 h, and characterized using XRD. The XRD patterns in Fig. 8(A) (state I) and 8C (state III) show slower α-to-δ

degradation, confirming the absence of the cracks. In contrast, faster α-to-δ degradation is observed in the cracked thin film (state II) in Fig. 8(B). Note that results from parallel experiments in $MAPbI_3$ thin films, which also degrade (typically to PbI_2) upon exposure to humid environment, were inconclusive. This is because the σ_R present in uncracked $MAPbI_3$ thin films, which is absent in α-$FAPbI_3$ thin films, can also accelerate moisture-induced degradation [39,40]. Thus, the effect of cracking alone on the degradation cannot be isolated in the case of $MAPbI_3$ thin films.

All the results demonstrate the generality of the crack-healing phenomenon in OIHPs, although it is found to be more facile in $MAPbI_3$ compared to α-$FAPbI_3$, which may be related to the higher formation energy of α-$FAPbI_3$ [14,15].

4. Discussion

The interesting cracking-healing observations in OIHP thin films can be explained based on the fundamentals of brittle fracture. The original Griffith theory of brittle fracture is couched in thermodynamics, where for equilibrium fracture to occur, the decrease in the mechanical energy (U_M) of the system is balanced exactly by the corresponding increase in the surface energy (U_S) of the material [25]: $dU/dC = 0$, where $dU = dU_M + dU_S$ and dC is the infinitesimal crack area (length $dc \times$ unit width). Here dU_M and dU_S identify with $-GdC$ and $+G_C dC$, respectively, where G is the applied strain energy release rate. In an *in vacuo* closed system, G_C is the same as the specific surface energy of the material, $2\gamma_S$ [25]. (In the case of intergranular fracture in a polycrystalline material, $G_C = 2\gamma_S - \gamma_{GB}$, where γ_{GB} is the grain boundary energy [25]). Thus, in such an ideal situation, the crack will propagate when $dU/dC0$ (loading), but implicit in the Griffith theory is the fact that the crack will retract and heal when $dU/dC>0$ upon unloading [25]. However, in real systems, there are several dissipative elements that can prevent cracks from healing completely upon full unloading of the external load, some of which that are relevant to thin films are listed as follows [25]. First, relaxation of any residual stresses that may be present can prevent the cracks walls from coming in contact despite full unloading. Second, atomic and/or molecular species from the atmosphere can adsorb onto fresh fracture surfaces, which are trapped when the crack walls are brought back together in contact. Third, there is always slight misalignment between the two relaxed mating crack-wall surfaces, compared to the original material before fracture, when they come together in contact upon unloading during healing. (Small bits of material and other debris can also fall in between the crack walls during the fracture process, which can serve as 'wedges' when the crack walls come together for healing. However, this effect is relevant to bulk materials, not thin films, where the cracks are deep and crack-mouth openings wide.) Thus, additional energy is needed to force the crack walls together in intimate contact, and to drive mass-transport across that contact for restoring the chemical bonds and heal the cracks [25]. Furthermore, the healed crack is now an 'interface,' and not 'pristine' material, which may comprise relaxed/misoriented lattice and trapped atoms/molecules from the environment. If the specific energy associated with that new 'interface' is γ_i, then the energy of the overall healed crack is $G_C' = G_C - \gamma_i$. This energy-landscape discussion is depicted schematically in Fig. 9(A), where the difference between the free energy of the healed system (G_C') and the unhealed system (G_C), γ_i, represents the driving force for crack-healing. The activation energy, E_A, is then provided by a combination of compressive stress (applied or CTE-mismatch induced) and temperature (room temperature or elevated temperature). By corollary, the healed crack 'interface' will have a lower toughness compared to the 'pristine' material.

This mechanism is illustrated schematically in Fig. 9(B)–(F), where Fig. 9(B) depicts the as-deposited $MAPbI_3$ thin film with the in-plane biaxial tensile residual stress (σ_R), which is absent in the α-$FAPbI_3$ thin film. Upon the application of external uniaxial tensile stress (σ_T) during bending, the film fractures at multiple locations when the applied strain energy release rate $G \geq G_C$ (Fig. 9(C)). The experimental evidence (Fig. 4) has shown that the cracking relaxes the σ_R in $MAPbI_3$ (Fig. 9(D)). Due to the reasons mentioned above, upon unloading, the cracks are not healed, in both $MAbI_3$ and α-$FAPbI_3$ thin films. In the case of mechanical-healing, an externally applied compressive stress $\sigma_C = -214$ MPa is sufficient to bring the crack walls in intimate contact in both $MAPbI_3$ and α-$FAPbI_3$ thin films. Restoration of chemical bonding can then occur as a result of stress-induced, thermally-activated ionic-diffusion across the closed interface (Fig. 9(E)), which is sufficiently rapid at room temperature in OIHPs [33–36]. The time-dependence experiments (Fig. 6) confirm the thermally-activated nature of the crack-healing process. In the case of thermal-healing, where no external compression is applied, the CTE-mismatch compressive stress σ_H is estimated at −79 MPa for $MAPbI_3$ (ΔT = 23–100 °C) using Eq. (3). In the case of α-$FAPbI_3$, assuming the same E and α_{OIHP} values, σ_H is estimated at −118 MPa (ΔT = (23–140 °C)), where the α-to-δ phase transformation is not occurring during the heat-treatment. These internal compressive stresses induced due to the heat-treatment (Fig. 9(E)) are lower than the applied stress of $\sigma_C = -214$ MPa in the room-temperature mechanical-healing case, but the higher temperature is expected to accelerate ion-diffusion, resulting in the crack healing in the OIHP thin films (Fig. 9(F)), and the restoration of the tensile residual stresses in the case of $MAPbI_3$.

The allure of regaining the mechanical integrity of cracked brittle materials has driven sporadic studies of crack healing for almost a century. The earliest report of crack healing in brittle materials by Oberimoff dates back to 1930, where cleaving and healing of mica was studied [25,41]. While most of the later studies were focused on bulk oxide ceramics and glasses, where heat-treatments at very high temperatures were used to heal cracks [42,43], there have been only a couple of low-temperature crack-healing studies on all-inorganic halides such as KCl, KBr, and LiF [44,45]. For example, in KCl, a compressive stress was used to partially heal large cracks in bulk KCl single-crystals at room temperature, where about 20–25% of the initial K_{IC} is regained in the healed crystals depending on the loading rate (time-dependent) [45]. While this healing effect is modest, it was found to be more pronounced in irradiated KCl single-crystals containing higher concentration of point defects [45]. These results indicate that ionic-diffusion, which is facilitated by point defects, plays a key role in crack-healing in KCl. It is likely that similar mechanisms are at play in the crack-healing of OIHP thin films with its even higher point-defects concentration and more facile ionic diffusion compared to all-inorganic halides [33–36].

The formation of through-thickness vertical cracks in the brittle OIHP thin film due to the various sources of internal and external stresses certainly compromises the integrity of the PSCs, leading to the degradation of their performance, environmental stability, and mechanical reliability. More importantly, these vertical cracks provide a proliferation of internal free-surfaces, which, over time, facilitate the nucleation and propagation of the more damaging horizontal delamination cracks at the interfaces between the OIHP thin film and the other layers. In this context, the crack-healing of OIHP thin films demonstrated here, which is based on inherent material behavior, can be combined with more engineering approaches, such as shifting of neutral-axis in bending [46]. This is likely to have broad implications for preventing and/or restoring the overall performance, environmental stability, and mechanical reliability of PSCs. Thus, in the context of OIHPs, the following axiom may be stated: what is easy to 'make' (solution-processing), is easy to 'break' (fracture), but is also easy to 'fix' (crack-healing). This axiom is equally applicable to other interesting 'healing' phenomena observed in OIHPs [47–49].

6. Summary

The facile healing of through-thickness cracks induced by bending-tension in thin films of two prototypical OIHPs, $MAPbI_3$ and α-$FAPbI_3$, is demonstrated. This is through the application of either a moderate compressive stress (bending-compression) at room temperature or a simple heat-treatment at moderate temperatures. Crack-healing is confirmed by SEM observations in both $MAPbI_3$ and α-$FAPbI_3$ thin films. In addition, XRD techniques are used to confirm crack-healing: the restoration of CTE-mismatch residual stresses in $MAPbI_3$ thin films and the diminished environmental degradation in α-$FAPbI_3$ thin films. In both OIHP thin films, the crack-healing process is found to be time-dependent, which indicates that facile mass-transport in OIHPs plays a key role in this phenomenon. The crack-healing mechanisms in OIHP thin films are explained based on the fundamentals of brittle fracture. This discovery of facile crack-healing in OIHP thin films has broad implications for the prevention and/or restoration of the overall performance, environmental stability, and mechanical reliability of PSCs, and other devices, as they are poised for commercialization.

Declaration of Competing Interest

The authors declare that they have no known competing financial interests or personal relationships that could have appeared to influence the work reported in this paper.

Acknowledgments

The support for this research at Brown University from the Office of Naval Research (N00014-17-1-2232) and the National Science Foundation (OIA-1538893) is gratefully acknowledged. This research used resources of the Advanced Photon Source, a Department of Energy Office of Science User Facility operated by Argonne National Laboratory (DE-AC02-06CH11357).

Supplementary materials

Supplementary material associated with this article can be found in the online version at doi:10.1016/j.actamat.2020.01.040.

References

[1] B. Saparov, D.B. Mitzi, Organic-inorganic perovskites: structural versatility for multifunctional materials design, Chem. Rev. 116 (2016) 4558–4596.
[2] N.-G. Park, M. Grätzel, T. Miyasaka, Organic–Inorganic Halide Perovskite Photovoltaics: From Fundamentals to Device Architectures, Springer, Zurich, Switzerland, 2016.
[3] Z. Xiao, Y. Yan, Progress in theoretical study of metal halide perovskite solar cells materials, Adv. Energy Mater. 7 (2017) 1701136.
[4] H.J. Snaith, Present status and future prospects of perovskite photovoltaics, Nat. Mater 17 (2018) 372–376.
[5] A.K. Jena, A. Kulkarni, T. Miyasaka, Halide perovskite photovoltaics: background, status, and future prospects, Chem. Rev . 119 (2019) 3026–3103.
[6] NREL, https://www.nrel.gov/pv/cell-efficiency.html, accessed on September 1, 2019.
[7] T.C. Sum, N. Mathews, Halide Perovskites: Photovoltaics, Light Emitting Diodes and Beyond, Wiley-VCH, Weinheim, Germany, 2019.
[8] Z.-K. Tan, R.S. Moghaddam, M.L. Lai, P. Docampo, R. Higler, F. Deschler, M. Price, A. Sadhanaia, L.M. Pazos, D. Credgington, F. Hanusch, T. Bein, H.J. Snaith, R.H. Friend, Bright light-emitting diodes based on organometal halide perovskite, Nat. Nanotechnol. 9 (2014) 687–692.
[9] G. Xing, N. Matthews, S.S. Lim, N. Yantara, X. Liu, D. Sabba, M. Graetzel, S. Mhaisalkar, T.C. Sum, Low-temperature solution-processed wavelength-tunable perovskites for lasing, Nat. Mater. 13 (2014) 476–480.
[10] L. Dou, Y. Yang, J. You, Z. Hong, W.-H. Chang, G. Li, Y. Yang, Solution-processed hybrid perovskite photodetectors with high detectivity, Nat. Comm 5 (2014) 5404.
[11] S. Yakunin, M. Sytnyk, D. Kriegner, S. Shrestha, M. Richter, G.J. Matt, H. Azimi, C. Brabec, J. Stangl, M.V. Kovalenko, W. Heiss, Detection of X-ray photos by solution-processed lead halide perovskites, Nat. Photon 9 (2015) 444–449.
[12] Q. Dong, Y. Fang, Y. Shao, P. Mulligan, J. Qiu, L. Cao, J. Huang, Electron-hole diffusion lengths >175 μm in solution-growth $CH_3NH_3PbI_3$ single crystals, Science 347 (2015) 967–970.
[13] W.A. Dunlop-Shohl, Y. Zhou, N.P. Padture, D.B. Mitzi, Synthetic approaches for halide perovskite thin films, Chem. Rev. 119 (2019) 3193–3295.
[14] G.P. Nagabhushana, R. Shivaramaiah, A. Navrotsky, Direct calorimetric verification of thermodynamic instability of lead halide hybrid perovskites, Proc. Natl. Acad. Sci. 113 (2016) 7717–7721.
[15] I.L. Ivanov, A.S. Steparuk, M.S. Bolyachkina, D.S. Tsvetkov, A.P. Safronov, A.Y. Zuev, Thermodynamics of formation of hybrid perovskite-type methylammonium lead halides, J. Chem. Thermodyn. 116 (2018) 253–258.
[16] C.C. Boyd, R. Cheacharoen, T. Leijtens, M.D. McGehee, Understanding degradation mechanisms and improving stability of perovskite photovoltaics, Chem. Rev 119 (2019) 3418–3451.
[17] Y. Rong, Y. Hu, A. Mei, H. Tran, M.I. Saidaminov, S.I. Seok, M. McGehee, E.H. Sargent, H. Han, Challenges for commercializing perovskite solar cells, Science 361 (2018) 1214.
[18] Z. Li, T.R. Klein, D.H. Kim, M.J. Yang, J.J. Berry, M.F.A.M. van Hest, K. Zhu, Scalable fabrication of perovskite solar cells, Nat. Rev. Mater. 3 (2018) 18017.
[19] N. Rolston, B.L. Watson, C.D. Bailie, M.D. McGehee, J.P. Bastos, R. Gehlhaar, J.-E. Kim, D. Vak, A.T. Mallajosyula, G. Gupta, A.D. Mohite, R.H. Dauskardt, Mechanical integrity of solution-processed perovskite solar cells, Extreme Mech. Lett. 9 (2016) 353–358.
[20] M.A. Reyes-Martinez, A.L. Abdelhady, M.I. Saidaminov, D.Y. Chung, O.K. Bakr, M.G. Kanatzidis, W.O. Soboyejo, Y.-L. Loo, Time-dependent mechanical response of $APbX_3$ (A = Cs, CH3NH3; X = I, Br) single crystals, Adv. Mater. 29 (2017) 1606556.
[21] C. Ramirez, S.K. Yadavalli, H.F. Garcces, Y. Zhou, N.P. Padture, Thermo-mechanical behavior of organic-inorganic halide perovskites for solar cells, Scr. Mater 150 (2018) 36–41.
[22] N. Rolston, A.D. Printz, J.M. Tracy, H.C. Weerasinghe, D. Vak, L.J. Haur, A. Priyadarshi, N. Mathews, D.J. Slotcavage, M.D. McGehee, R.E. Kalan, K. Zielinski, R.L. Grimm, H. Tsai, W. Nie, A.D. Mohite, S. Gholipour, M. Saliba, M. Grätzel, R.H. Dauskardt, Effect of cation composition on the mechanical stability of perovskite solar cells, Adv. Energy Mater. 8 (2018) 1702116.
[23] Y. Rakita, S.R. Cohen, N.K. Kedem, G. Hodes, D. Cahen, Mechanical properties of $APbX_3$ (A = Cs or CH_3NH_3; X = I or Br) perovskite single crystals, MRS Commun. 5 (2015) 623–629.
[24] S. Sun, F.H. Isikgor, Z. Deng, F. Wei, G. Kieslich, P.D. Bristowe, J. Ouyang, A.K. Cheetham, Factors influencing the mechanical properties of formamidinium lead halides and related hybrid perovskites, ChemSusChem 10 (2017) 3740–3745.
[25] B.R. Lawn, Fracture of Brittle Solids, 2nd ed., Cambridge University Press, Cambridge, U.K., 1993.
[26] N.J. Jeon, J.H. Noh, Y.C. Kim, W.S. Yang, S. Ryu, S.I. Seok, Solvent engineering for high-performance inorganic-organic hybrid perovskite solar cells, Nat. Mater 9 (2014) 897–903.
[27] J.-W. Lee, Z. Dai, C. Lee, H.M. Lee, T.-H. Han, N.D. Marco, O. Lin, C.S. Choi, B. Dunn, J. Koh, D.D. Carlo, J.H. Ko, H.D. Maynard, Y. Yang, Tuning molecular interactions for highly reproducible and efficient formamidinium perovskite solar cells *via* adduct approach, J. Am. Chem. Soc. 140 (2018) 6317–6324.
[28] B.D. Cullity, Elements of X-ray Diffraction, 2nd edition, Addison-Wesley, Boston, MA, 1978.
[29] M. Birkholz, Thin Film Analysis by X-ray Scattering, Wiley-VCH, Berlin, 2006.
[30] N. Klein-Kedem, D. Cahen, G. Hodes, Effects of light and electron beam irradiation on halide perovskites and their solar cells, Acc. Chem. Res. 49 (2016) 347–354.
[31] T.J. Jacobsson, L.J. Schwan, M. Ottosson, A. Hagfeldt, T. Edvinsson, Determination of thermal expansion coefficients and locating the temperature-induced phase transition in methylammonium lead perovskites using x-ray diffraction, Inorg. Chem. 54 (2015) 10678–10685.
[32] C.-H. Chien, T. Chen, F.-I. Su, C.-Y. Lin, T.-H. Su, Y.-M. Lin, Y.-C. Liu, T.-L. Tsay, Thickness effects on the thermal expansion coefficient of indium tin oxide/polyethylene terephthalate film, Expt. Technol. 40 (2016) 639–644.
[33] Y. Yuan, J. Huang, Ion migration in organometal trihalide perovskite and its impact on photovoltaic efficiency and stability, Acc. Chem. Res. 49 (2016) 286–293.
[34] H. Wang, A. Guerrero, A. Bou, A.M. Al-Mayouf, J. Bisquert, Kinetic and material properties of interfaces governing slow response and long timescale phenomena in perovskite solar cells, Energy Environ. Sci. 12 (2019) 2054–2079.
[35] T.-Y. Yang, G. Gregori, N. Pellet, M. Grätzel, J. Maier, The significance of ion conduction in a hybrid organic–inorganic lead–iodide–based perovskite photosensitizer, Angew. Chem. Int. Ed. 54 (2015) 7905–7910.
[36] A. Senocrate, I. Moudrakovski, G.Y. Kim, T.-Y. Yang, G. Gregori, M. Grätzel, J. Maier, The nature of ion conduction in methylammonium lead iodide: a multimethod approach, Angew. Chem. Int. Ed. 56 (2017) 7755–7759.
[37] G.E. Eperon, S.D. Stranks, C. Menelaou, M.B. Johnston, L.M. Herz, H.J. Snaith, Formamidinium lead trihalide: a broadly tunable perovskite for efficient planar heterojunction solar cells, Energy Environ. Sci. 7 (2014) 982–988.
[38] S. Prathapani, D. Choudhary, S. Mallick, P. Bhargava, A. Yella, Experimental evaluation of room temperature crystallization and phase evolution of hybrid perovskite materials, CrystEngComm 19 (2017) 3834–3843.
[39] J. Zhao, Y. Deng, H. Wei, X. Zheng, Z. Yu, Y. Shao, J.E. Shield, J. Huang, Strained hybrid perovskite thin films and their impact on the intrinsic stability of perovskite solar cells, Sci. Adv. 3 (2017) eaao5616.
[40] N. Rolston, K.A. Bush, A.D. Printz, A. Gold-Parker, Y. Ding, M.F. Toney, M.D. McGehee, R.H. Dauskardt, Engineering stress in perovskite solar cells to improve stability, Adv. Energy Mater. 8 (2018) 1802139.
[41] J.W. Obreimoff, The splitting strength of mica, Proc. R. Soc. A 217 (1930) 290–297.
[42] C.C. Yu, C.B. Lin, S. Lee, Theory for the rate of crrack closure, J. Appl. Phys. 78 (1995) 212–216.
[43] P. Greil, Generic principles of crack-healing ceramics, J. Adv. Ceram. 1 (2012) 249–267.

[44] L. Wagner, S. Lee, J.C.M. Li, Mechanical healing of ionic crystals, Scr. Metall. 4 (1985) 361–365.
[45] S.M. Jang, S. Lee, Mechanical healing of potassium chloride single crystals, J. Am. Ceram. Soc. 73 (1990) 659–664.
[46] G. Lee, M.-C. Kim, Y.W. Choi, N. Ahn, J. Jang, J. Yoon, S.M. Kim, J.-G. Lee, D. Kang, H.S. Jung, M. Choi, Ultra-flexible perovskite solar cells with crumpling durability: toward a wearable power source, Energy Environ. Sci. 12 (2019) 3182–3191.
[47] Z. Zhou, Z. Wang, Y. Zhou, S. Pang, D. Wang, H. Xu, Z. Liu, N.P. Padture, G. Cui, Methylamine-gas-induced defect-healing behavior of $CH_3NH_3PbI_3$ thin films for perovskite solar cells, Angew. Chem. Int. Ed. 54 (2015) 9705–9709.
[48] Y. Zhou, N.P. Padture, Gas-induced formation/transformation of organic–inorganic halide perovskites, ACS Energy Lett. 2 (2017) 2166–2176.
[49] D. Cahen, I. Lubomirsky, Self-repairing energy materials: *sine qua non* for a sustainable future, Acc. Chem. Res. 50 (2017) 573–576.